# Prediction of two-dimensional 2H-M$_2$O$_3$ (M=Ti and Zr) with strong linear and non-linear optical response in infrared range (Supporting Information)

Anqi Huang,[1] Linxuan Ji,[1] Qiaoqiao Li, [1]Yu Wu,[2] Yi-min Ding,[2,*] and Liujiang Zhou[1,2,†]

[1] *School of Physics, State Key Laboratory of Electronic Thin Films and Integrated Devices, University of Electronic Science and Technology of China, Chengdu 610054, China*

[2] *Yangtze Delta Region Institute (Huzhou), University of Electronic Science and Technology of China, Huzhou 313001, China*

∗ ymding00@qq.com
† ljzhou@uestc.edu.cn

**Details for Real-time approach to nonlinear optical properties**

Nonlinear optical properties are obtained within the real-time (RT) approach developed by Attaccalite et.al.[1–3] In this approach the time-dependent Schrödinger equation is integrated to obtain the time-dependent valence states $|v_{mk}\rangle$, shown as:

$$i\hbar \frac{d}{dt}|v_{mk}\rangle = \left(H_{\mathbf{k}}^{sys} + i\mathcal{E} \cdot \tilde{\partial}_{\mathbf{k}}\right)| \tag{1}$$

Herein $|v_{mk}\rangle$, $H_{\mathbf{k}}^{sys}$ is the system Hamiltonian—which is discussed later; $\mathcal{E} \cdot \tilde{\partial}_{\mathbf{k}}$ describes the coupling with the external field in the dipole approximation. While the Born-vonarmar periodic boundary conditions are imposed, the coupling takes the form of a $\mathbf{k}$-derivative operator $\tilde{\partial}_{\mathbf{k}}$. The tilde indicates that the operator is 'gauge covariant' and guarantees that the solutions of eqn (1) are invariant under unitary rotations among occupied states at $\mathbf{k}$.

From $|v_{mk}\rangle$, the time-dependent polarization of the system $P_{\parallel}$ along the lattice vector a is calculated as,

$$P_{\parallel} = -\frac{ef|\mathbf{a}|}{2\pi v N_{\mathbf{k}_{\perp}}} \sum_{\mathbf{k}_{\perp}} \mathrm{Imlog} \prod_{\mathbf{k}_{\parallel}}^{N_{\mathbf{k}_{\parallel}}-1} detS(\mathbf{k}, \mathbf{k} + \mathbf{q}_{\parallel}) \tag{2}$$

where $S(\mathbf{k}, \mathbf{k} + \mathbf{q}_{\parallel})$ is the overlap matrix between $|v_{nk}\rangle$ and $|v_{mk+\mathbf{q}_{\parallel}}\rangle$. Furthermore, $v$ is the unit cell volume, $f$ is the spin degeneracy, $N_{\mathbf{k}_{\perp}}$ and $N_{\mathbf{k}_{\parallel}}$ are respectively the number of $\mathbf{k}$ points along and perpendicular to the polarization direction, and $\mathbf{q}_{\parallel} = 2\pi/(N_{\mathbf{k}_{\parallel}}\mathbf{a})$. Finally, the second harmonic coe-cient is extracted from the power series of the polarization in the laser field $\mathcal{E}$, $\mathbf{P} = \chi^{(1)}\mathcal{E} + \chi^{(2)}\mathcal{E}\mathcal{E} + \chi^{(3)}\mathcal{E}\mathcal{E}\mathcal{E} + \cdots$

In eqn (1), the model Hamiltonian chosen for $H_{\mathbf{k}}^{sys}$, determines the level of approximation in the description of correlation effects in the SHG spectra. In this work, two different models for the system Hamiltonian are adopted: (i) the independent-particle approximation (IPA) model and (ii) the real-time GW + BSE model. In IPA, the system Hamiltonian is simply evaluated from the Kohn-Sham DFT Hamiltonian with $G_0W_0$ corrections by a scissor operator,

$$H_{\mathbf{k}}^{sys} = H_{\mathbf{k}}^{DFT} + \sum_{nk} \Delta_{nk}|v_{nk}^0\rangle\langle v_{nk}^0| \tag{3}$$

where $\Delta_{nk} = E_{nk}^{G_0W_0} - E_{nk}^{DFT}$. This model is named as IPA-$G_0W_0$ for simplicity in the main text. In RT-GW+BSE model,

$$H_{\mathbf{k}}^{sys} = H_{\mathbf{k}}^{DFT} + \sum_{nk} \Delta_{nk}|v_{nk}^0\rangle\langle v_{nk}^0| + V_h(\mathbf{r})[\Delta\rho] + \Sigma_{SEX}[\Delta\gamma] \tag{4}$$

where $\Delta\rho \equiv \rho(r;t) - \rho(r;t=0)$ is the variation of the electronic density and $\Delta\gamma \equiv \gamma(r, r';t) - \gamma(r, r';t = 0)$ is the variation of the density matrix induced by the external field $\mathcal{E}$. $V_h(\mathbf{r})[\Delta\rho]$ is the Hartree potential and is responsible for the local-field effects originating from system inhomogeneities. The last term $\Sigma_{SEX}[\Delta\gamma]$, is the screened-exchange self-energy that accounts for the electron-hole interaction, and is given by the convolution between the screened interaction W and $\Delta\gamma$. In the linear response limit, the GW+BSE model reproduces the optical absorption calculated by solving the BetheSalpeter equation. [4] This model is named as RT-$G_0W_0$+BSE for simplicity in the main text. The EOM, Eq.(1), can be numerically solved for |vmk⟩ using the following algorithm developed by Crank and Nicholson[5] for both Hermitian and non-Hermitian type Hamiltonians:

$$|v_{nk}(t + \Delta t)\rangle = \frac{I - i(\Delta t/2)\mathcal{H}_{\mathbf{k}}^{system}(t)}{I + i(\Delta t/2)\mathcal{H}_{\mathbf{k}}^{system}(t)}|v_{nk}(t)\rangle, \tag{5}$$

in which $I$ is the identity element. The operation is strictly unitary for any value of time-step $\Delta$t. It turns out that if the applied field is a Dirac $\delta$-type, the Fourier transformed responses can be

evaluated at all frequencies. In our simulations, we switch on the monochromatic field at t = $t_0$. This sudden switch excites the eigenfrequencies of the system introducing spurious contributions to the nonlinear response. An imaginary term is added into the Hamiltonian to simulate a finite dephasing,

$$\Gamma = -\frac{i}{\gamma_{deph}} \sum_l |v_{\mathbf{k},l}\rangle\langle v_{\mathbf{k},l}| - |v_{\mathbf{k},l}^0\rangle\langle v_{\mathbf{k},l}^0|\}, \qquad (6)$$

where $|v_{\mathbf{k},l}^0\rangle$ are the valence bands of the unperturbed system and $\gamma_{deph}$ is the dephasing rate. Then we run the simulations for a time much larger than $1/\gamma_{deph}$ and sample P(t) close to the end of the simulation. Since $\gamma_{deph}$ determines also the spectral broadening, we cannot choose it arbitrary small. The smaller the dephasing rate is, the longer the simulation is. As an empirical parameter, the dephasing time $1/\gamma_{deph}$ is usually set as 6.6 fs, which corresponds to a spectral broadening of approximately 0.2 eV.

Table S1. Elastic stiffness constants, Young's modulus (Y, N/m), Shear modulus (G, N/m), and Poisson ratio ($\nu$) of $Ti_2O_3$ and $Zr_2O_3$ monolayers.

| Systems | $C_{11}$ | $C_{12}$ | $C_{66}$ | Y | G | $\nu$ |
|---|---|---|---|---|---|---|
| $Ti_2O_3$ | 184.49 | 41.50 | 71.49 | 175.15 | 71.49 | 0.22 |
| $Zr_2O_3$ | 189.13 | 10.86 | 89.13 | 188.50 | 89.13 | 0.06 |

Table S2. Effective masses of $Ti_2O_3$ and $Zr_2O_3$ in unit of $m_0$.

| | Electron | | Hole | |
|---|---|---|---|---|
| Ti2O3 | $\Gamma\rightarrow$K | 1.02 | $\Gamma\rightarrow$K | -0.62 |
| | $\Gamma\rightarrow$M | 1.00 | $\Gamma\rightarrow$M | -0.61 |
| Zr2O3 | K$\rightarrow\Gamma$ | 0.34 | K$\rightarrow\Gamma$ | -0.77 |
| | K$\rightarrow$M | 0.36 | K$\rightarrow$M | -0.83 |

Table S3. SHG coefficients (pm/V) of single-layer $MoS_2$, $Ti_2O$, $Zr_2O_3$ and $NbOCl_2$ at different wavelengths.

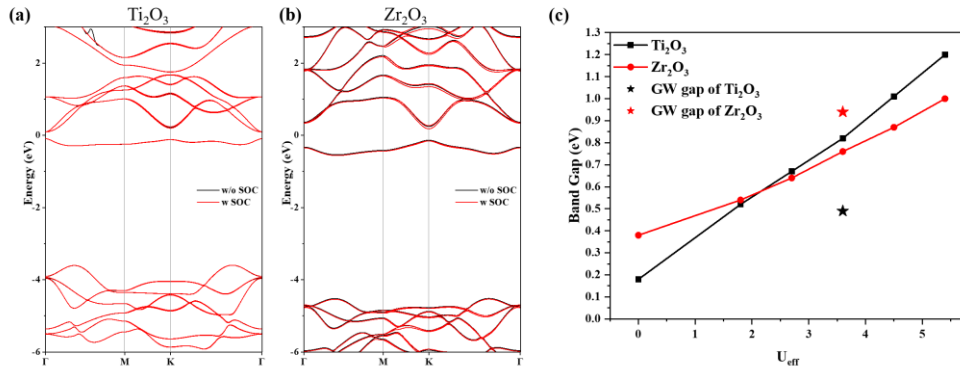| | 1360 nm | 1400 nm | 1480 nm | 1560 nm |
|---|---|---|---|---|
| $MoS_2$ | 282.1 | 153.7 | 44.7 | 24.2 |
| $Ti_2O_3$ | 231.0 | 311.2 | 316.2 | 377.7 |
| $Zr_2O_3$ | 1552.4 | 1630.0 | 1541.3 | 1395.7 |
| $NbOCl_2$ | 58.6 | 56.7 | 56 | 55 |



Figure S1. Band structures of 2H-$Ti_2O_3$ (a) and 2H-$Zr_2O_3$ (b) with and without SOC. Variation of band gap from DFT+U method with Ueff values (c). The band gap form the GW method is shown.
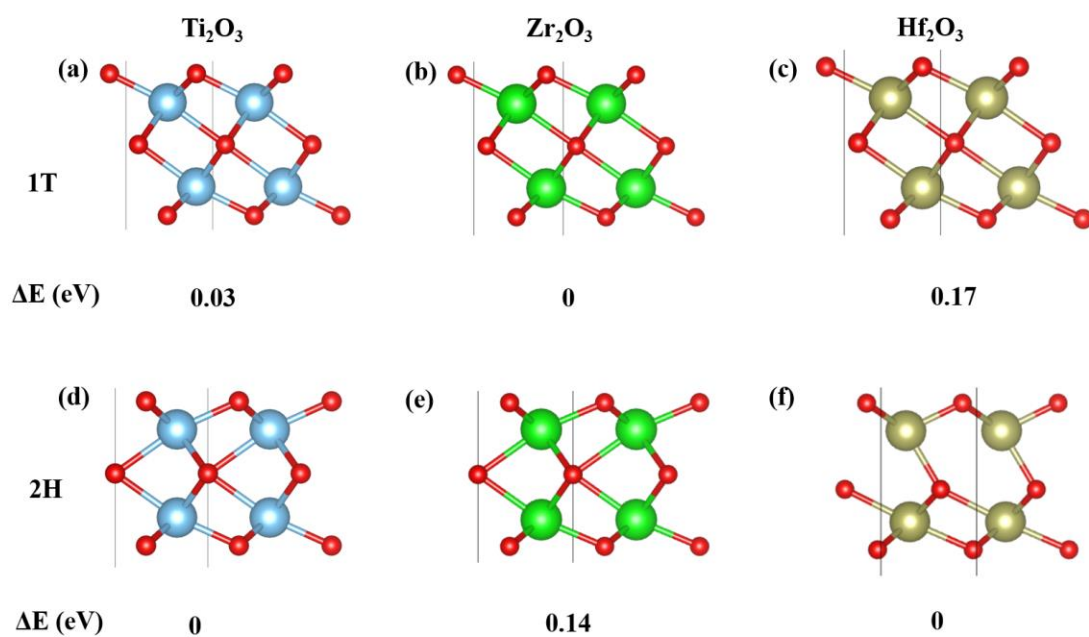
Figure S2. The most stable configurations and relative energies after relaxation for (a-c) 1T-M$_2$O$_3$ and (d-f) 2H-M$_2$O$_3$(M=Ti, Zr, Hf).
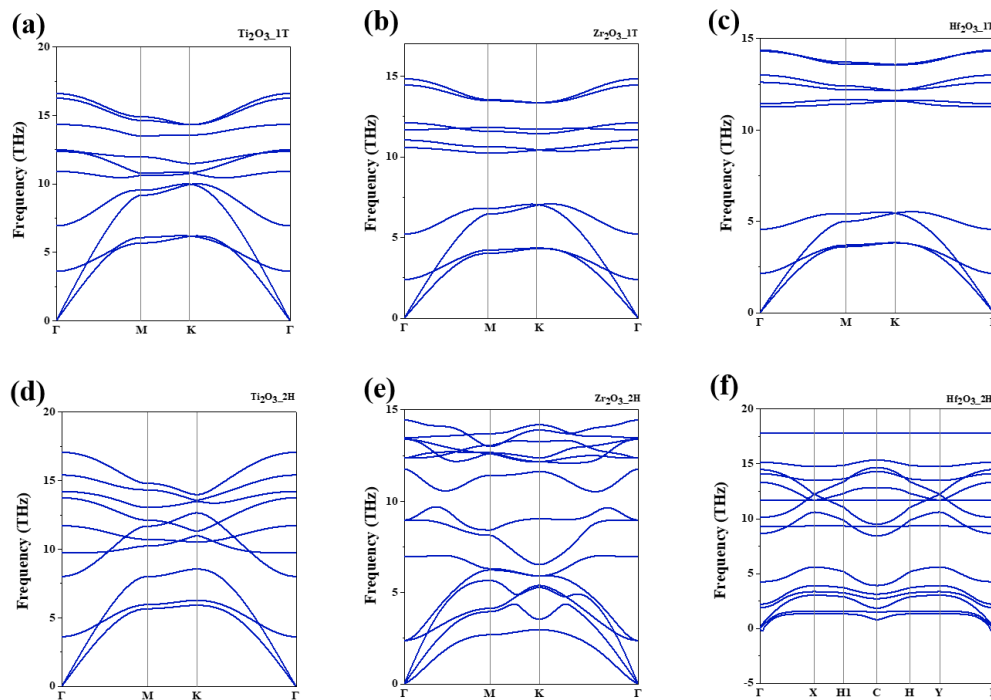


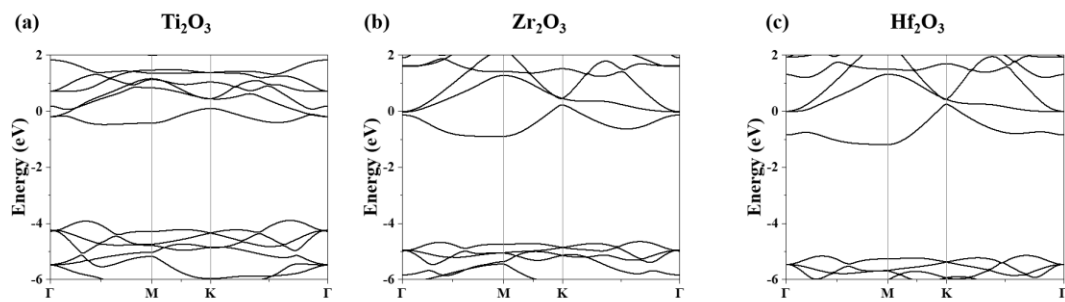Figure S3. Phonon spectrum of (a-c) 1T and (e-f) 2H-M$_2$O$_3$(M = Ti, Zr, Hf).

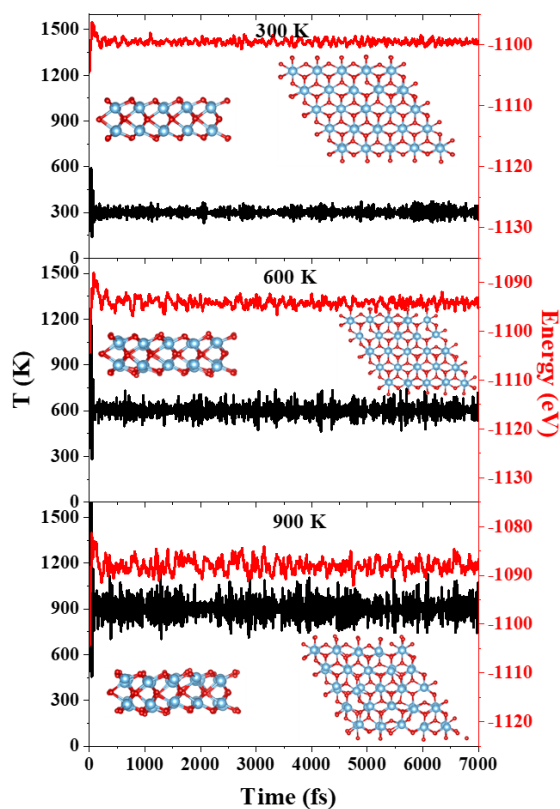Figure S4. Band structure of (a) 1T-Ti$_2$O$_3$, (b) 1T-Zr$_2$O$_3$,and (c) 1T-Hf$_2$O$_3$.



Figure S5. Energy and temperature changes of Ti$_2$O$_3$ during the 300/600/900 K AIMD simulation, and final snapshots of side and top views.
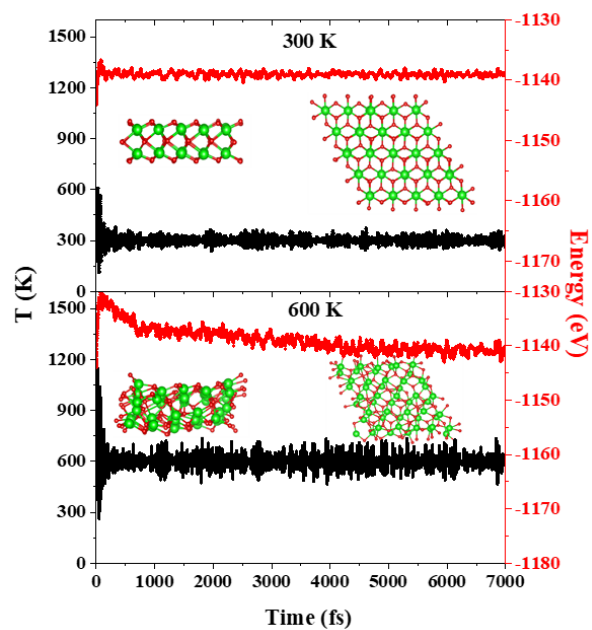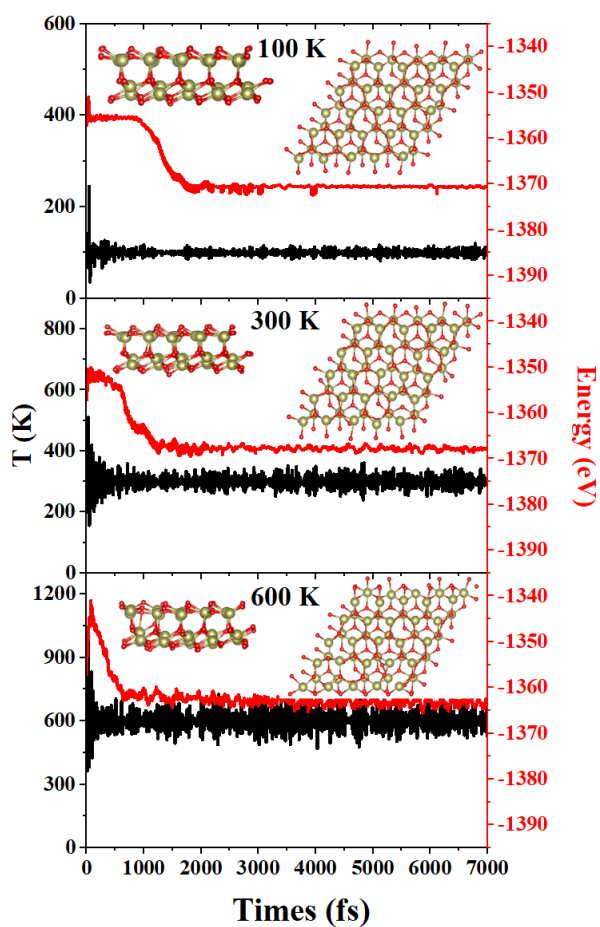
Figure S6. Energy and temperature changes of $Zr_2O_3$ during the 300/600 K AIMD simulation, and final snapshots of side and top views.



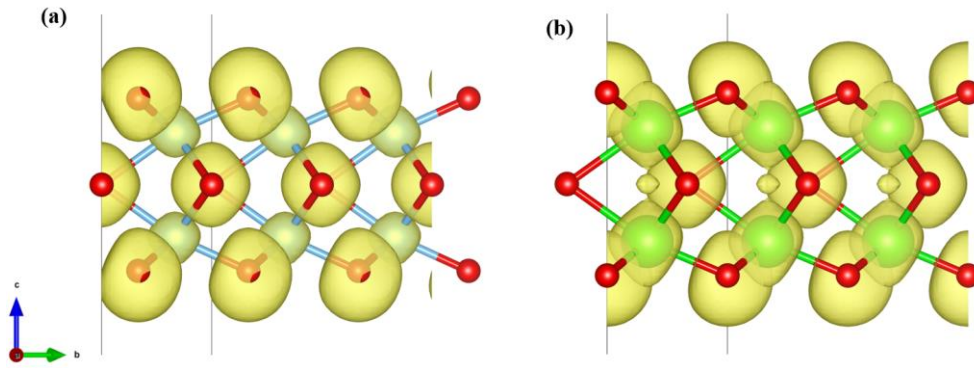Figure S7. Energy and temperature changes of $Hf_2O_3$ during the 100/300/600 K AIMD simulation, and final snapshots of side and top views.

Figure S8. Plots of the ELF of (a) $Ti_2O_3$ and (b) $Zr_2O_3$ monolayers. The isosurface value is 0.01 Bohr/$Å^3$.
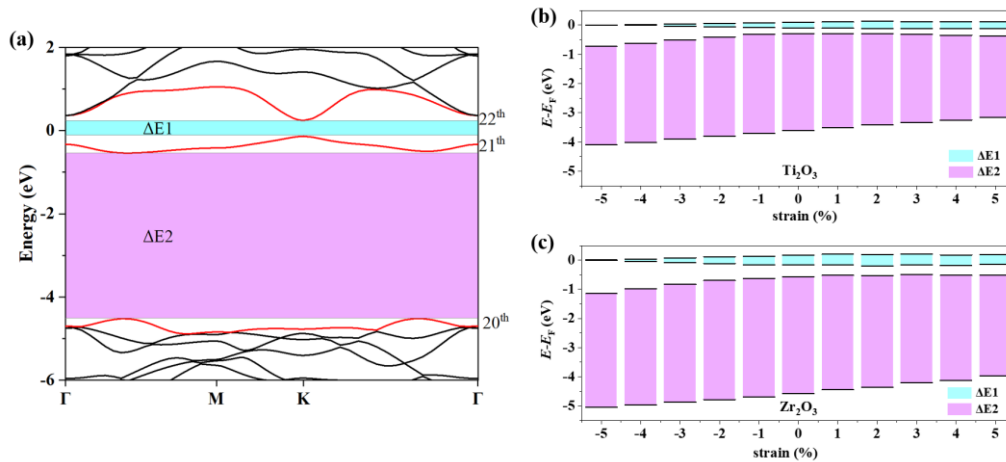


Figure S9. Schematic representation of energy gaps, $\Delta E1$ and $\Delta E2$, in the band structure (a), as well as the position of the band edges and the two energy gaps of (b) 2H-$Ti_2O_3$ and (c) 2H-$Zr_2O_3$ as a function of strain.
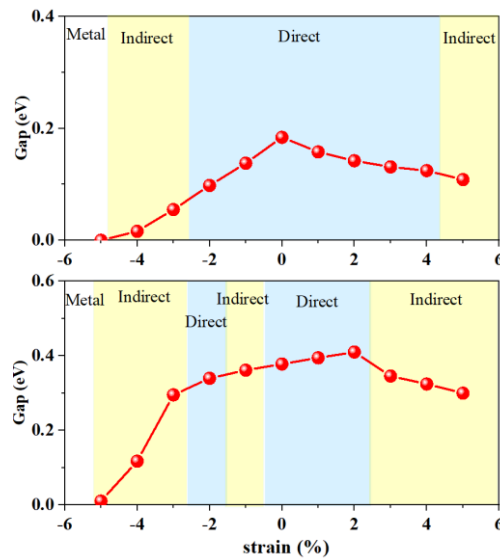


Figure S10. Variation of the energy gap from DFT-PBE as a function of uniaxial strain at different points of high symmetry in 2H-$Ti_2O_3$ and 2H-$Zr_2O_3$ monolayers. Yellow, blue, and white represent indirect gap, direct gap, and metallic properties,

respectively.



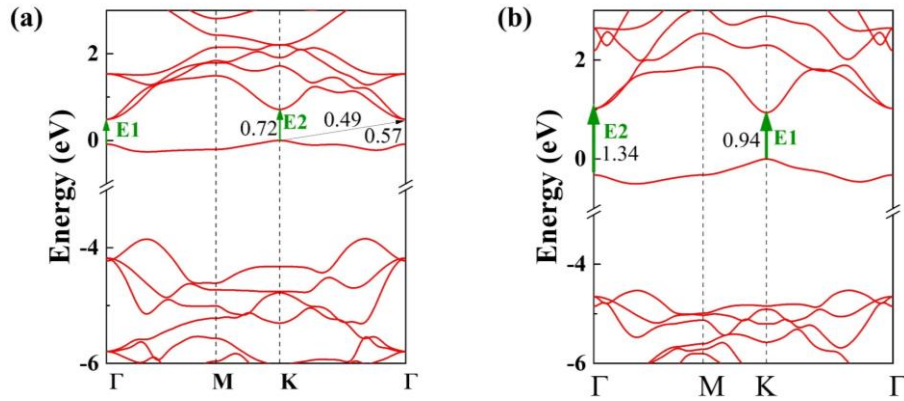Figure S11. Band structures of 2H-Ti$_2$O$_3$ (a) and 2H-Zr$_2$O$_3$ (b) monolayers were calculated using the G$_0$W$_0$ method.
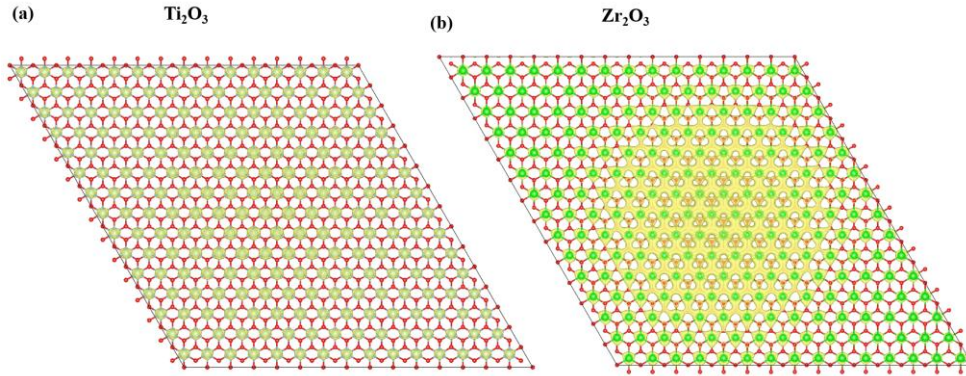


Figure S12. Real-space wave functions of the lowest energy excitons for (a) 2H-Ti$_2$O$_3$ and (b) 2H-Zr$_2$O$_3$.
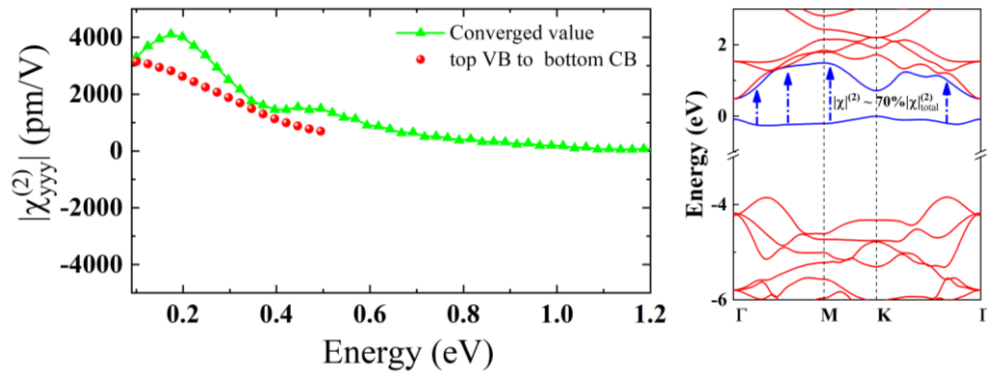


Figure S13. The absolute value of SHG coefficient for Ti$_2$O$_3$ with energy band considering top VB to bottom CB (red circle) and converged results (green triangle), and the schematic diagram of virtual transitions from top VB to bottom CB in the band structure.
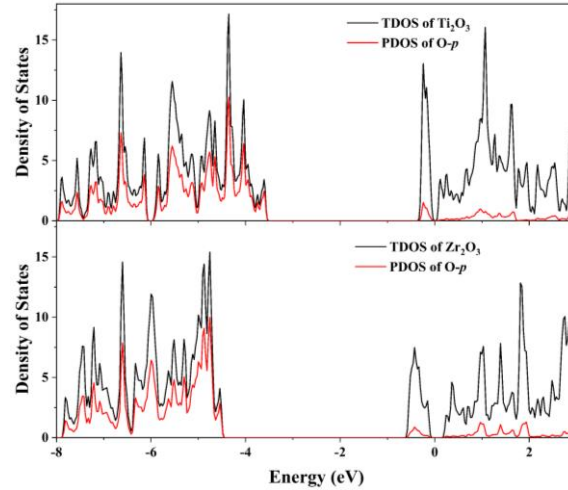
Figure S14. Total and projected densities of states of the *s* and *p* orbitals of the oxygen in 2H-Ti$_2$O$_3$ and 2H-Zr$_2$O$_3$.
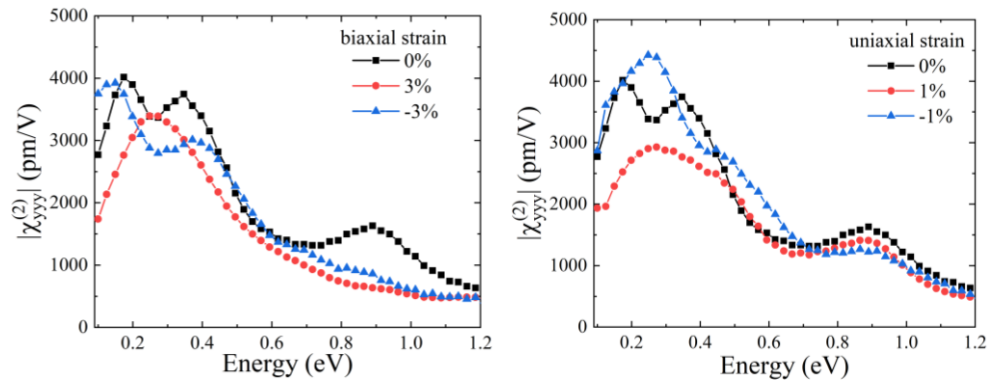


Figure S15. Absolute value of SHG coefficient of Zr$_2$O$_3$ under biaxial and uniaxial strains.

Reference:

1 C. Attaccalite and M. Grüning, *Phy. Rev. B*, 2013, **8**, 235113.

2 M. Grüning and C. Attaccalite, *Phys. Rev. B*, 2014, **89**, 081102.

3 C. Attaccalite, A. Nguer, E. Cannuccia and M. Grüning, *Phys. Chem. Chem. Phys.*, 2015, **17**, 9533–9540.

4 C. Attaccalite, M. Grüning and A. Marini, *Phys. Rev. B*, 2011, **84**, 245110.

5 J. Crank and P. Nicolson, *Adv. Comput Math*, 1996, **6**, 207–226.